# Topographic Trapping of the Leeuwin Current and Its Impact on the 2010/11 Ningaloo Niño

XUE FENG,[a] TOSHIAKI SHINODA,[a] AND WEIQING HAN[b]

[a] *Texas A&M University—Corpus Christi, Corpus Christi, Texas*
[b] *University of Colorado Boulder, Boulder, Colorado*

(Manuscript received 4 April 2022, in final form 1 November 2022)

ABSTRACT: Previous theoretical studies suggest that the topography along the west coast of Australia plays an important role in strengthening and trapping the Leeuwin Current (LC) at the coast. To isolate and quantify the effect of the continental shelf and slope on the LC and Ningaloo Niño, high-resolution (1/12°) ocean general circulation model experiments with different bottom topographies are performed. The "*control*" experiment uses a realistic bottom topography along the west coast of Australia, whereas the sensitivity ("*no-shelf*") experiment uses a modified topography with no continental shelf and slope near the coast. The mean and variability of LC are realistically simulated in the *control* experiment. Compared to the *control* experiment, the strength of LC in the *no-shelf* experiment decreased by about 28%. The continental shelf influences the development of the 2010/11 Ningaloo Niño through modulating the LC variability: in August–October 2010 and January–February 2011, the LC in the *control* experiment is enhanced much more than that in the *no-shelf* experiment. As a result, the upper-50-m ocean temperature in the *control* experiment is about 26% warmer than the *no-shelf* experiment from September 2010 to March 2011. Different evolution of SST warming is also found in the two experiments. Comparisons of oceanic processes in the two experiments show that the shelf-slope topography can effectively trap the positive sea level anomaly at the coast in the *control* experiment while more Rossby waves radiate from the coast in the *no-shelf* experiment, resulting in a weaker LC.

KEYWORDS: Indian Ocean; Topographic effects; Boundary currents; Heat wave; Climate variability; Ocean models

## 1. Introduction

The Leeuwin Current (LC) is a narrow eastern boundary current flowing along the west coast of Australia (e.g., Cresswell and Golding 1980; Thompson 1984; Smith et al. 1991). Compared to other eastern boundary currents, it is unique in that the current flows poleward against the prevailing wind direction (e.g., Godfrey and Ridgway 1985; McCreary et al. 1986; Godfrey and Weaver 1991). Observations show that the average speed of the LC is about 30 cm $s^{-1}$, and the LC becomes stronger in austral autumn and winter, during which the speed exceeds 55 cm $s^{-1}$ (Smith et al. 1991; Feng et al. 2003). The LC variability largely contributes to the southeast Indian Ocean heat balance because it advects warm waters from the tropics to the west coast of Australia, and thus it strongly impacts regional climate variability such as the Ningaloo Niño (Feng et al. 2013) and local biodiversity and fishery (Wernberg et al. 2013).

A prominent feature of the LC is that the strong current is coastally trapped near the shelf break, and the current is associated with a high sea level at the coast and a strong cross-shore pressure gradient. Hence, to maintain the strong LC, some physical processes must exist to prevent the high sea level along the coast from radiating offshore as Rossby waves. Several mechanisms have been proposed to explain the trapping of the LC along the coast. For example, Kundu and McCreary (1986) suggested that the Rossby waves are damped by vertical diffusion near the coast, and thus the high sea level cannot be radiated too far from the coast. However, the model required an unrealistically large vertical mixing coefficient to generate a coastally trapped LC, with an amplitude weaker than observations. Weaver and Middleton (1989, 1990) demonstrated that the continental shelf can provide a trapping mechanism. In their analytical model, the ocean was represented by a two-layer system with a linear shelf profile at the eastern boundary. Given a fixed alongshore density gradient, the model generated a trapped current with realistic speed over the continental slope. The alongshore current cannot be formed without a continental slope due to the Rossby wave radiation. However, the speed of the LC largely depended on the bottom friction coefficient, and the assumption of $\beta = 0$ (constant Coriolis parameter) in the shelf region eliminates the Rossby wave genesis. Hence the role of the continental shelf in LC trapping is still inconclusive in their study.

Recent studies by Furue et al. (2013) and Benthuysen et al. (2014b) examined the major coastal processes that are responsible for the coastal trapping of the LC in detail and showed that the presence of a continental slope is necessary to generate realistic LC strength and structure. In Furue et al. (2013), the linear model used by Weaver and Middleton (1989, 1990) was modified by including $\beta$ with more realistic model layer formulations and neglecting mixing, bottom friction, and advection. The results demonstrated that the characteristic curves of Rossby waves bend southward in the coastal region due to the topographic beta effect, and thus the LC is trapped over the slope. Because there is no friction to damp Rossby waves in the model, the main factor that accounts for the trapping of the LC is the sloping bottom topography. Benthuysen et al. (2014b) obtained similar results using an idealized numerical

*Corresponding author*: Xue Feng, xfeng2@islander.tamucc.edu

DOI: 10.1175/JCLI-D-22-0218.1

model, which includes all the neglected processes in Furue et al. (2013). Without the shelf-slope topography, the simulated LC at equilibrium was about 2 cm $s^{-1}$, which is too weak compared with observations. By including the shelf and slope at the eastern boundary, the LC speed increased substantially to about 25 cm $s^{-1}$, demonstrating the important role of the continental shelf in maintaining the LC strength.

While the theoretical studies described above have provided sufficient evidence that the existence of continental shelf-slope is crucial for trapping and strengthening the LC, their results are based on models with highly idealized shelf and forcings, Hence, it is difficult to determine to what extent the coastal topography affects the observed LC strength and variability. Accordingly, it is necessary to use models with realistic topography and forcings for isolating the effect of topography on the LC.

Since the LC strongly influences regional and global climate variability through the advection of warm waters from the tropics, the continental shelf and slope may play an important role in climate variability such as the Ningaloo Niño by changing the LC evolution. For example, during the 2010/11 Ningaloo Niño event, the anomalous surface warming associated with a surge of the LC was observed in the coastal regions of Western Australia. The upper ocean warming peaked in February–March 2011 and the sea surface temperature (SST) in some regions was ~5°C warmer than the climatological mean (Pearce and Feng 2013; Feng et al. 2013). By the end of 2010, large easterly anomalies in the equatorial Pacific Ocean, which is associated with the strong 2010/11 La Niña, forced positive sea level anomalies in the western Pacific Ocean. Because the sea level along the west coast of Australia is highly correlated with the western equatorial Pacific Ocean at one month lag (Feng et al. 2013), the remote Pacific forcing could accelerate the LC through oceanic wave propagation. In addition, negative sea level pressure dominated the southeast Indian Ocean during the peak phase. The associated northerly wind anomalies reduced the climatological southeasterly, thereby strengthening the LC. Hence the anomalous poleward heat advection caused by the enhanced LC plays a dominant role in the 2010/11 Ningaloo Niño (Feng et al. 2013; Benthuysen et al. 2014a; Marshall et al. 2015).

Previous numerical modeling studies on the Ningaloo Niño have focused on the mechanisms for the development of anomalous ocean warming (e.g., Marshall et al. 2015; Kataoka et al. 2017; Zhang et al. 2018). However, detailed physical and dynamical processes that are responsible for the LC enhancement during the Ningaloo Niño, including the role of the continental slope, are still unclear. Given the importance of remote forcing for Ningaloo Niño development, models with a larger domain that includes the Pacific Ocean basin are required to examine the role of the oceanic processes in the evolution of Ningaloo Niño. In addition, the use of a high horizontal resolution model is crucial for simulating realistic LC speed since the model needs to adequately resolve the narrow width of LC and the sloping shelf (e.g., Godfrey and Weaver 1991; Furue 2019).

In this study, a high-resolution Indo-Pacific basin ocean general circulation model (OGCM) is used to evaluate and quantify the influences of the shelf-slope on the LC structures and strength. The sensitivity experiment is designed to isolate the effect of the bottom topography on the LC strength and variability. Also, the outputs of these experiments are further analyzed to investigate the role of the continental slope in the evolution of the Ningaloo Niño. While the major processes that cause ocean warming during the Ningaloo Niño vary from event to event (e.g., Marshall et al. 2015; Zhang et al. 2018; Feng and Shinoda 2019), the anomalous surge of LC plays a dominant role in the 2010/11 extreme event (Feng et al. 2013; Benthuysen et al. 2014a). Hence, this study focuses on discussing the oceanic processes during the 2010/11 Ningaloo Niño.

The rest of the paper is organized as follows. Section 2 introduces the OGCM experiments and data used in this study. Section 3 presents the model results including the effects of sloping topography on the LC, the analysis for the 2010/11 Ningaloo Niño period, and the role of the continental shelf-slope in the evolution of Ningaloo Niño through changes in LC development. Finally, section 4 provides a summary and discussion.

## 2. Model experiments and validation

### a. *OGCM experiments*

The OGCM used in this study is the Hybrid Coordinate Ocean Model, version 2.2.98 (HYCOM; Bleck 2002). The model is configured on a Mercator grid from 10°N to 55°S and from 10°E to 67°W, which covers the equatorial and southern Indian and Pacific Oceans. The horizontal grid spacing is 1/12°. There are 40 layers in the vertical, among which 14 layers are set to hybrid $z$–sigma layers to better resolve the shelf and mixed layer processes and the layer thickness gradually increases from 1 m (top layer) to 8 m (layer 14). Relaxation boundary conditions are used at the north, south, and west boundaries. A sponge layer with 20 grid points is used, in which the model temperature and salinity are relaxed to Polar Science Center Hydrographic Climatology (PHC) 3.0 (Steele et al. 2001) with the relaxation time scale varying from 3 to 95 days. The bottom topography is adapted from the 30-arc-s General Bathymetric Chart of the Oceans (GEBCO; Weatherall et al. 2015). Additional hand editing based on a combination of navigational charts and scientific literature was performed in the Indonesian Seas to improve the representation of the Indonesian Throughflow (Metzger et al. 2010). Model experiment with these realistic bottom topographies is referred to as the "*control*" experiment hereafter.

In addition to the *control* experiment, a sensitivity experiment with modified bottom topography has been conducted to isolate the effect of the continental shelf along the west coast of Australia on upper ocean processes. In the sensitivity experiment, the bottom topography near the west coast of Australia between 22° and 35°S was replaced by a flat bottom at 2000 m and a vertical wall along the coastline. This experiment is referred to as the "*no-shelf*" experiment hereafter. The bottom topography used in the *control* and *no-shelf* experiments is shown in Fig. 1. The difference between the *control* and *no-shelf* experiments represents the influence of the continental shelf

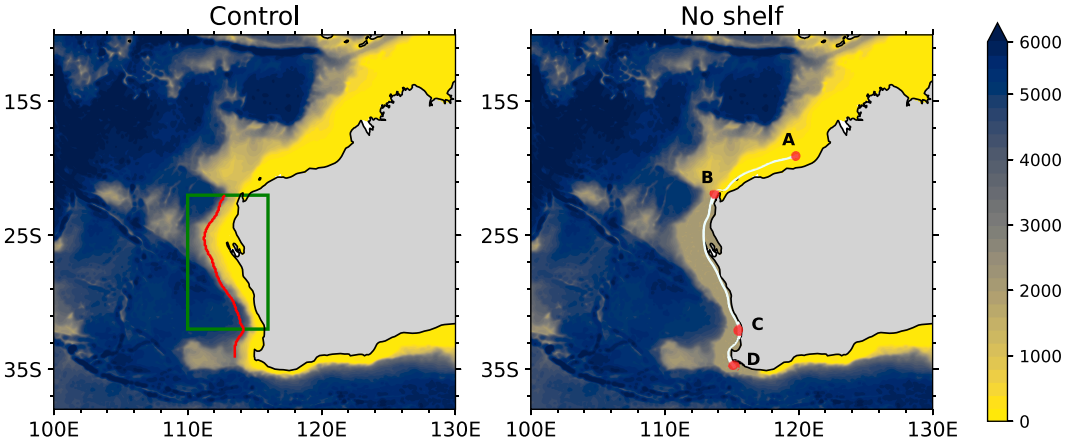


FIG. 1. Bathymetry (m) of the (left) *control* and (right) *no-shelf* experiments. The green rectangle in the left panel indicates the Ningaloo Niño Index (NNI) region, and the red line denotes the western edge of the LC. The white line in the right panel shows the coastal waveguide from point A in the northwestern Australian shelf (20°S, 120°E) to point D near Cape Leeuwin (35°S, 150°E), and the waveguide generally follows the 100 m isobath in the *control* experiment. Points B and C indicate the locations of the reference lines used in Fig. 12.

along the west coast of Australia on upper ocean variability, including the LC and its impact on SST near the coast.

Surface forcing fields derived from ERA5 (Hersbach et al. 2018) are used in both the *control* and *no-shelf* experiments. Surface latent and sensible heat fluxes are computed using the CORE v2 bulk flux algorithm (Large and Yeager 2004). Since this study examines the impact of LC-induced heat advection on SSTs, the specific humidity and air temperature are calculated as a function of model SSTs. If the observed specific humidity (from reanalysis) is used in OGCM experiments, the model SST is very close to observations, especially in midlatitudes where the mean winds are stronger than in the tropics (e.g., Seager et al. 1995; Shinoda and Lin 2009). In this case, the impact of LC variations on SST cannot be properly simulated and quantified by OGCM experiments. Hence, in this study the air temperature ($T_a$) and specific humidity ($q_a$) at 2 m used in the bulk flux algorithm are calculated from the model SST using the following empirical formula:

$$T_a = \mathrm{SST} - \Delta T,$$

$$q_a = \mathrm{Rh} \times q_s(T_a), \qquad (1)$$

where $\Delta T$ is the difference between SST and $T_a$, Rh is relativity humidity, and $q_s(T_a)$ is the saturation specific humidity at $T_a$. Monthly climatological values of $\Delta T$ and Rh at each location are estimated using SST, $T_a$ and Rh from the WHOI Objectively Analyzed Ocean–Atmosphere Flux (OAFlux) product (Yu et al. 2008) for the period 1985–2016. In this manner, the SST is freely evolved in response to the variation of oceanic processes such as the heat advection produced by LC variability.

The method described above was originally developed by Waliser and Graham (1993) in which $\Delta T$ and Rh are constant and thus appropriate for the tropics. Because of the spatially varying $\Delta T$ and Rh in Eq. (1), the method generates reasonable estimates of latent and sensible heat fluxes for larger domains including the southeast Indian Ocean. Yet the method is much more computationally efficient compared to other more complex formulations (Seager et al. 1995; Deremble et al. 2013). The reconstructed air humidity using Eq. (1) agrees well with those estimated by Deremble et al. (2013). It is also worth pointing out that $\Delta T$ and Rh have a much broader spatial structure than the LC; hence, it is unlikely that they impact artificially on the dynamical processes along the coast.

With the above configurations of surface forcing fields, the model was spun up for 20 years from a state of rest with monthly climatological forcing from ERA5. Then, the model is integrated forward from 2002 to 2015 with daily forcing fields from ERA5. The daily outputs for 2004–15 are analyzed. The *control* and *no-shelf* experiments use identical surface forcing fields and thus only the difference in bottom topography is responsible for the difference in model results between the two experiments.

### b. Data and analysis

Multiple SST products are used to describe the SST variations during the Ningaloo Niño and to compare with the *control* experiment. These are daily SSTs from the NOAA Optimum Interpolation (OI) Sea Surface Temperature (OISST v2) analysis (Reynolds et al. 2007) with the 0.25° resolution, the Operational Sea Surface Temperature and Sea Ice Analysis (OSTIA) with the 0.05° resolution (Donlon et al. 2012), the Multi-Scale Ultra-High Resolution (MUR) product with the 0.01° resolution, the Remote Sensing Systems (REMSS) OI SST product with the 0.25° resolution, and monthly SST from the Tropical Rainfall Measuring Mission (TRMM) Microwave Imager (TMI) with the 0.25° resolution.

The satellite altimetry data distributed by Archiving, Validation, and Interpretation of Satellite Oceanographic (AVISO) are used to investigate the sea surface height (SSH) variability in the southeast Indian Ocean. AVISO data with a horizontal resolution of 0.25° × 0.25° for the period 2004–15 are used.

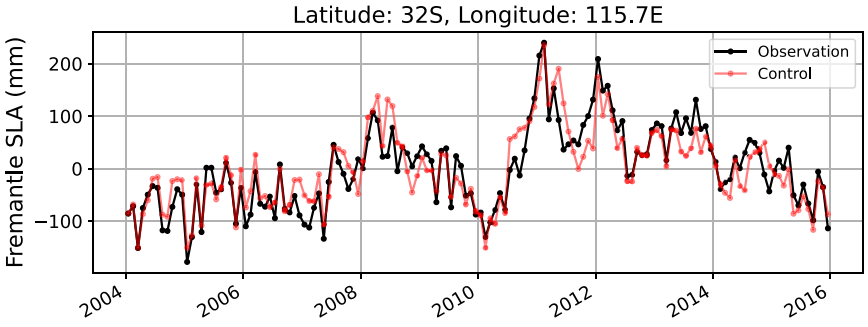


FIG. 2. Monthly Fremantle sea level anomalies from the *control* experiment and the tide gauge observation. Values at the grid point closest to the tide gauge station in the model are used.

The sea level at Fremantle (32.05°S, 115.72°E) measured by tide gauge is used as a proxy for the LC strength (Feng et al. 2003). The data for the period of 2004–15, which are obtained from University of Hawaii Sea Level Center, are used to validate the interannual variability of the simulated LC.

### c. *Validation*

The monthly sea level anomaly at Fremantle from the *control* experiment is compared with observations (Fig. 2). The simulated Fremantle sea level anomaly is highly correlated with the tidal gauge observation with a correlation coefficient of 0.90, indicating that the LC variability is realistically simulated in the *control* experiment.

To evaluate the evolution of the 2010/11 Ningaloo Niño in the *control* experiment, we use the Ningaloo Niño Index (NNI), which is the average SST anomalies over 22°–32°S, 110°–116°E (Marshall et al. 2015; box region in Fig. 1 herein), and the NNI derived from model outputs is compared with that from observations. Figure 3 shows that the timing of the development and decay of ocean warming including its peak in the *control* experiment agrees well with observations. However, the SST anomaly around the peak in January–March 2011 is somewhat underestimated. Nevertheless, the substantial SST warming associated with the 2010/11 Ningaloo Niño is well captured by the model, although the specific humidity from the reanalysis is not used in the latent heat flux calculation. Note that the range of the peak values in January 2011 in different datasets exceeds 1°C, revealing the uncertainty of the observed SSTs, and the peak value of model SST is very close to one of the datasets (OSTIA, within 0.2°C).

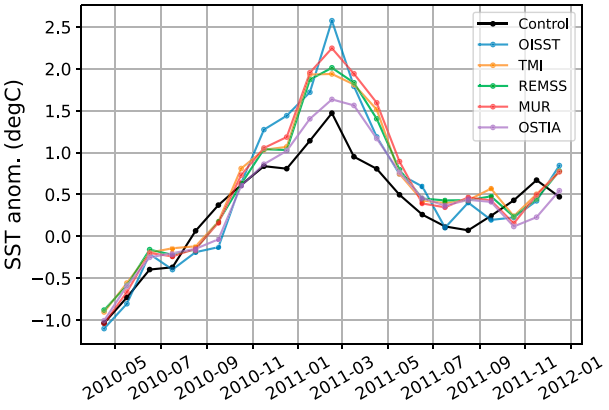


FIG. 3. Monthly SST anomalies averaged over the NNI region during the 2010/11 Ningaloo Niño.

## 3. Results

In this section, the mean and variability of the upper ocean including the LC in the *control* and *no-shelf* experiments are compared. Also, important oceanic processes, which cause the differences in the two experiments during the 2010/11 Ningaloo Niño, are identified and discussed.

### a. *Structure of the Leeuwin Current*

Figure 4 shows the average horizontal velocity over the upper 50 m for the period 2004–15. Many features of the LC in the *control* experiment (Fig. 4a) agree very well with observations (Feng et al. 2003; Furue et al. 2017). For example, the strong LC with the maximum southward velocity of about 20–30 cm $s^{-1}$ is evident around 32°S and the core of the LC is aligned with the shelf break. The LC accelerates toward the south and turns eastward after passing Cape Leeuwin, extending along the south coast of Australia.

In the *no-shelf* experiment, the LC is much weaker (Fig. 4b). To quantify the overall influence of the continental shelf-slope on the LC, the latitudinal average of meridional velocity in the large area is calculated. The meridional velocity at each latitude is first shifted zonally so that the western edges of the LC at all latitudes coincide. Here, the western edge of the LC (red line in Fig. 1) is defined as the location at 14 grid points (~1.12°) west of the 150 m isobath in the *control* experiment. Then the average values are calculated over the latitudinal range 22°–34°S. For comparison, the *no-shelf* experiment uses the same western edge of the LC as in the *control* experiment and the same zonal shift is applied. Figure 5 shows that the average core velocity of LC is reduced by about 28% due to the absence of the continental shelf in the *no-shelf* experiment. In addition to the differences in LC strength, the LC in the *no-shelf* experiment is located closer to the coastline than in the *control* experiment (Fig. 4) due to the removal of the continental shelf.

Figure 6 shows the vertical structure of the LC at 22°, 26°, 30°, and 34°S from the *control* and *no-shelf* experiments. In

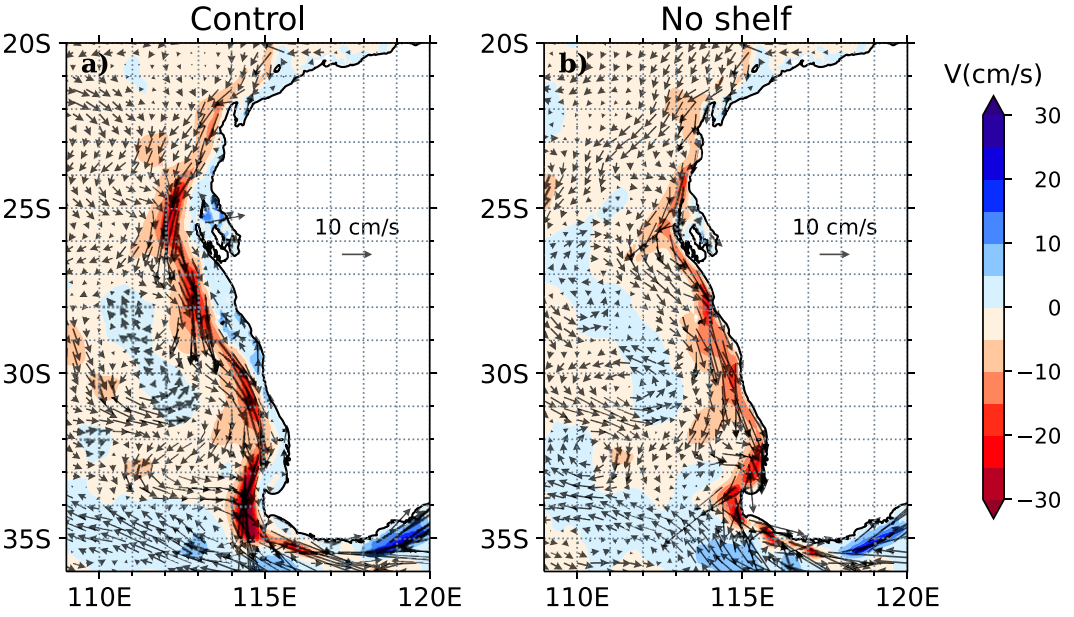


FIG. 4. Mean current averaged for the upper 50 m and for the period 2004–15: (a) *control* and (b) *no-shelf* experiments. The meridional velocity is shaded.

both experiments, the LC extends to a depth of 200–300 m, but a significant difference in the LC strength is observed, and the difference largely depends on the latitude. For example, the largest difference in the core velocity is found at 34°S, where the speed is 44 cm $s^{-1}$ in the *control* experiment and 26 cm $s^{-1}$ (41% weaker) in the *no-shelf* experiment. The core velocity is also significantly different at 22° and 26°S, but the difference is not as large as the one at 34°S. A reduction of 32% (27%) is found at 22°S (26°S) in the *no-shelf* experiment.

In summary, while the LC strength and location are well simulated in the *control* experiment, the LC in the *no-shelf* experiment is much weaker due to the lack of shelf-slope topography. The results highlight the importance of the topographic beta effect in the LC dynamics, which is consistent with the results from theoretical studies using idealized models (Furue et al. 2013; Benthuysen et al. 2014b). Yet the LC in our *no-shelf* experiment is much stronger than the no-shelf solution in Benthuysen et al. (2014b), suggesting that a variety of other processes may affect the generation and maintenance of the observed LC.

### b. *Evolution of the 2010/11 Ningaloo Niño*

The previous section demonstrated that the strength of the mean LC is largely affected by the continental shelf slope. Hence, large variations of the LC such as those observed during the 2010/11 Ningaloo Niño may also be influenced by the continental shelf-slope. Since the 2010/11 Ningaloo Niño is primarily driven by the heat advection associated with the

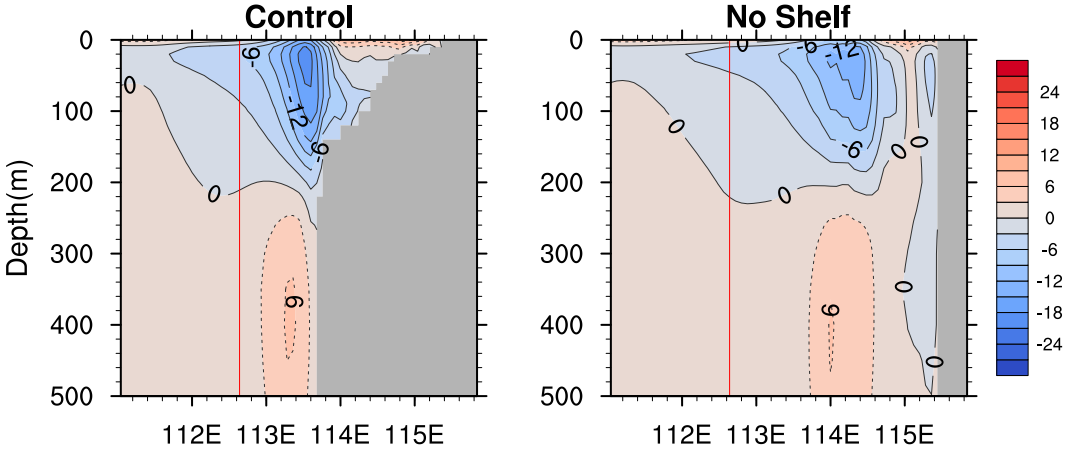


FIG. 5. The composite of the meridional velocities (cm $s^{-1}$) averaged over 22°–34°S from the (left) *control* and (right) *no-shelf* experiments. The red lines denote the western edge of the LC.

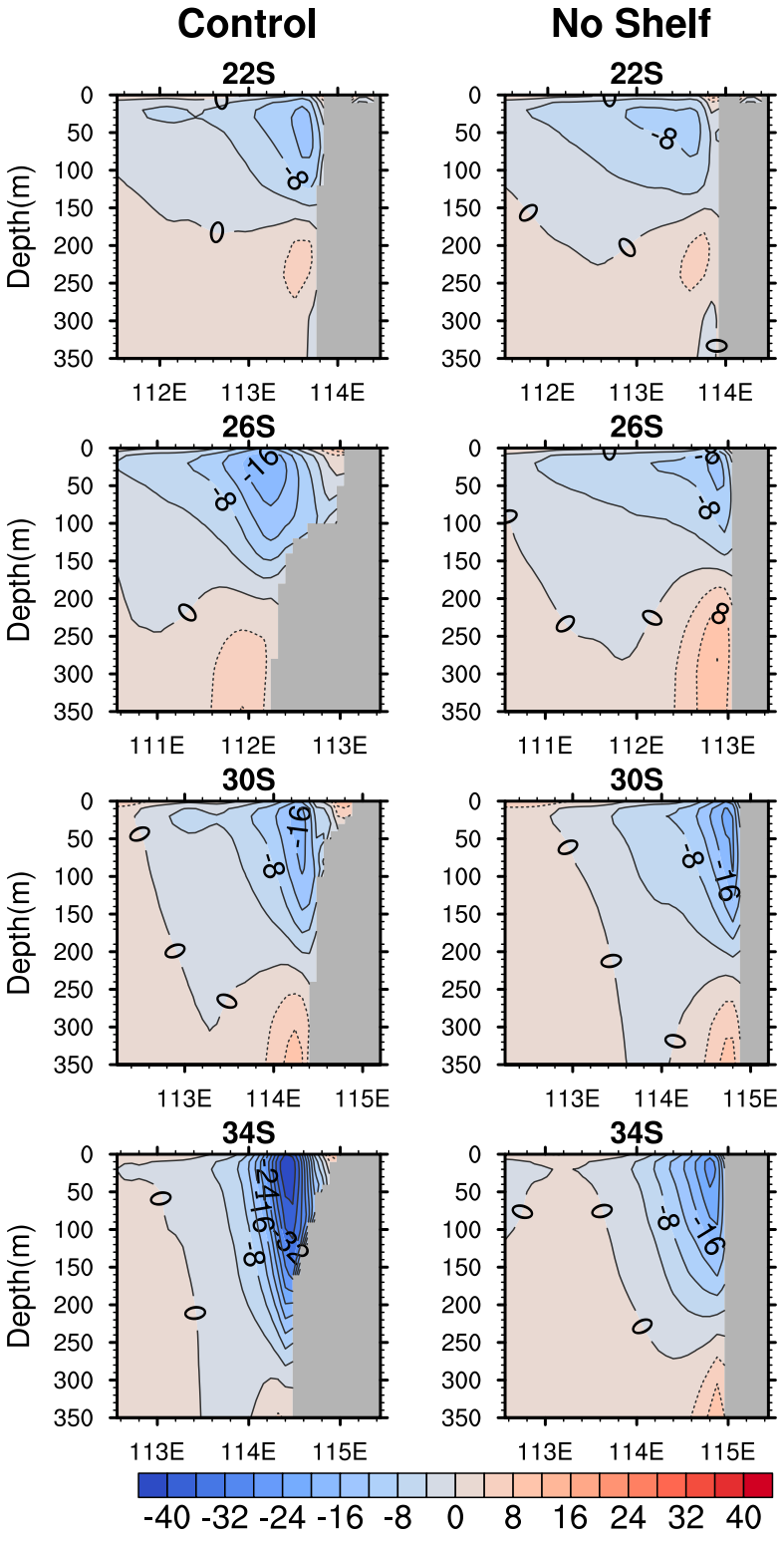


FIG. 6. Vertical structure of the LC (cm $s^{-1}$) at different latitudes—(from top to bottom) 22°, 26°, 30°, and 34°S—from the (left) *control* and (right) *no-shelf* experiments.

anomalous LC (Feng et al. 2013; Benthuysen et al. 2014a), the sloping coastal topography could provide a prominent influence on the evolution of the extreme warming. In this section, we examine how the LC evolution during the 2010/11 Ningaloo Niño is affected by the continental shelf slope and to what extent the LC variability during the event influences the SST warming.

Because of high eddy activities near the west coast of Australia, a large meander of the LC is frequently found, and thus the location of the LC core often deviates from that of the mean LC, which reveals an alongshore jet trapped near the coast (Fig. 4). Therefore, the LC variability is examined by using the southward velocity anomalies averaged in the NNI region. Figure 7 shows the time series of the upper-50-m LC anomaly during 2010/11. The surge of LC since April 2010 occurs in both the *control* and *no-shelf* experiments. While the acceleration of the LC in the *no-shelf* experiment slows down and ends in June 2010, the LC continues to grow in the *control* experiment and reaches the first peak in September 2010. After a short period of the LC decay (October–November), the velocity anomaly in the *control* experiment increases again in December 2010 and reaches the second peak in January 2011. Pronounced differences in the LC between the *control* and *no-shelf* experiments are found around September 2010, during which the anomalous LC in the *control* experiment is about 3 times stronger than that in the *no-shelf* experiment. Overall, the *no-shelf* experiment cannot produce prominent enhancements of the southward velocity anomaly during August 2010–February 2011, and the anomalous velocity is weaker than that in the *control* experiment during most of the warming period.

The strengthening of the LC during August–October 2010 is not forced by local winds because southerly wind anomalies are still dominant in the southeast Indian Ocean (Figs. 7. and 8). Therefore, the enhancement of the LC during this period is likely attributed to remotely forced coastal waves. In contrast, the subsequent enhancement of the LC around January 2011 (notable in the *control* experiment) is due to the development of northerly wind anomalies along the coast (Fig. 8).

The vertical structure of the meridional velocity anomaly shows that the strong southward current in the *control* experiment extends through the upper 50 m during the first LC enhancement (Fig. 7, middle panel), but the current is very weak in the *no-shelf* experiment with a core located around 20 m (Fig. 7, bottom panels). This suggests that the remotely forced component is very weak near the west coast of Australia when the continental shelf is absent. During the peak phase around January 2011, because the LC surge is driven by local winds, both the *control* and *no-shelf* experiments show relatively strong surface currents, but the currents in the *control* experiment are much stronger and extend deeper.

The evolution of simulated NNI from the *control* and *no-shelf* experiments is shown in Fig. 9 (black lines). The SST anomaly in the NNI region changes sign in August 2010, during which the LC speed increases sharply due to remote oceanic processes. Because the LC is much weaker in the *no-shelf* experiment, the development of anomalous ocean warming is delayed by about one month. By October 2010, the stronger LC in the *control* experiment causes a difference of about

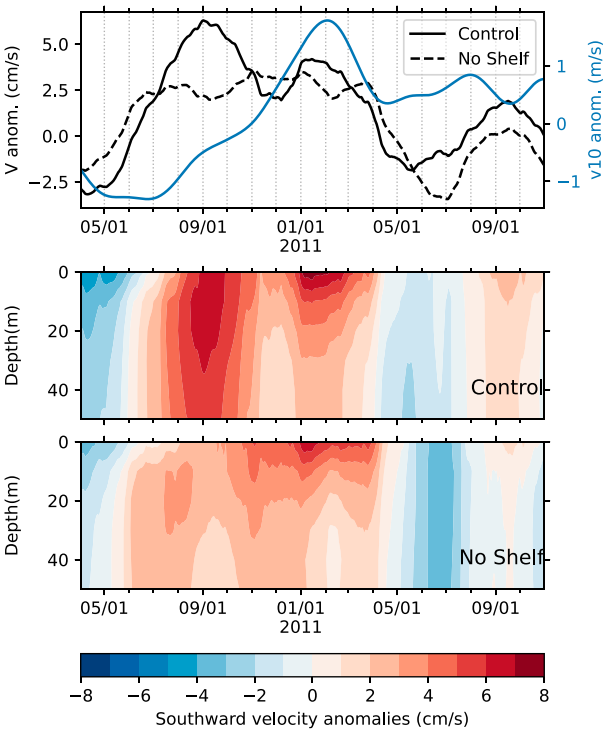


FIG. 7. Time series of southward velocity anomaly averaged over (top) the upper 50 m and its vertical distribution from the (middle) *control* and (bottom) *no-shelf* experiments. The 10 m wind anomaly time series is also shown in the top panel (blue solid line). The data have been smoothed with a 100-day lowpass filter. All anomalies are averaged over the NNI box region and positive values indicate southward.

0.5°C in the SST anomaly between the two experiments. Similarly, during the peak phase from January to March 2011, the anomalous SST in the *control* experiment is about 0.3°C warmer than that in the *no-shelf* experiment. The close relationship between the LC enhancement and SST warming in the two experiments demonstrates the important role of the continental shelf-slope in SST variability associated with the Ningaloo Niño through the large enhancement of the LC. To further confirm the role of continental shelf and LC in the SST warming, the average SST anomaly for the LC region, which is the area from the coastline to the western edge of the LC (red line in Fig. 1) and from 22° to 32°S, is also shown in Fig. 9 (red lines). The SST anomaly in the *control* experiment is larger than that in the *no-shelf* experiment for almost the entire period of positive anomaly from August 2010 to May 2011.

To explore the impact of the LC strength (and thus continental shelf) on the spatial pattern of ocean warming during the 2010/11 Ningaloo Niño, maps of SST anomalies at a 30-day interval from September 2010 to April 2011 are shown in Fig. 10. Here the SST anomalies are smoothed with a 100-day lowpass filter. In the *control* experiment, initial positive SST anomalies appear near the coast in early September. Much of the upper ocean warming is located near the coast during the entire period of the event while a portion of warm anomalies spreads to

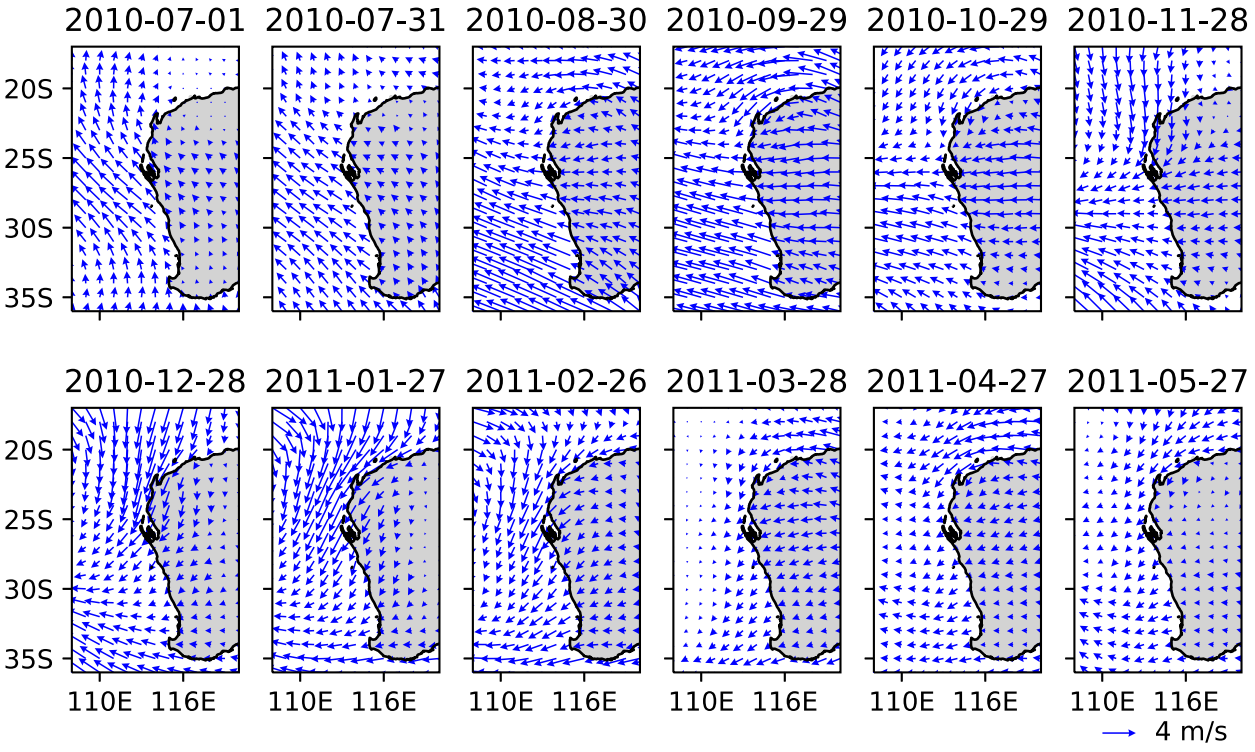


FIG. 8. Daily wind anomalies at 10 m from ERA5. The data have been smoothed with a 100-day lowpass filter.

the interior ocean by eddies and lateral mixings. During the peak phase, warm water extends southward, and the entire LC region is covered by large SST anomalies. In the *no-shelf* experiment, warming anomalies initially develop near the coast, but they tend to propagate westward during the development stage. From January to March 2011, coastal warming is still able to grow due to the wind-forced LC surge, but the magnitude of the warming is reduced because of the offshore propagation. Physical processes associated with the offshore propagation of SST anomalies will be further discussed in section 3c.

To further quantify the impact of LC enhancement induced by the topography on the Ningaloo Niño development, a heat budget analysis in the upper ocean for the NNI region is conducted (Fig. 11). Terms in the temperature equation are averaged from the surface down to 50 m as shown by the following equation:

$$\frac{1}{H}\int_H^0 \frac{\partial T}{\partial t}\,dz = \frac{Q_{\text{net}}}{\rho c_p H} - \frac{1}{H}\int_H^0 \mathbf{V}\cdot\nabla T\,dz + \text{res}, \qquad (2)$$

where $T$ is ocean temperature, $Q_{\text{net}}$ is the net air–sea heat flux, $H$ is 50 m, $\mathbf{V}$ is horizontal velocity vector, $\rho$ is the density of seawater, and $c_p$ is the specific heat of seawater. The first and second terms on the right-hand side of Eq. (2) represent the rate of temperature change due to surface heat fluxes and the horizontal heat advection (units: °C $s^{-1}$), respectively. The residual term includes the contributions from vertical advection and lateral and vertical mixings. The $Q_{\text{net}}$, $T$, and $\mathbf{V}$ are smoothed with a 100-day running mean to calculate the heat budget terms. Then the anomalies of terms in Eq. (2) are obtained by subtracting their climatology calculated from daily $Q_{\text{net}}$, $T$, and $\mathbf{V}$. The resulting anomalies are shown in Fig. 11, and data are presented in °C $\text{month}^{-1}$ for better visualization.

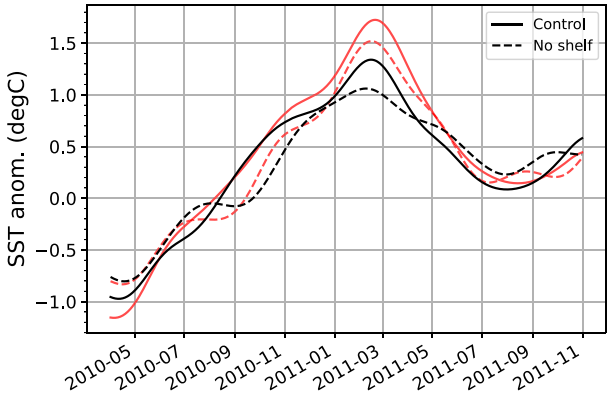


FIG. 9. Time series of the SST anomalies over the NNI region (black lines) and the LC region (red lines). The data have been smoothed with a 100-day lowpass filter.

Consistent with previous studies (e.g., Marshall et al. 2015), the anomalous warming in the 2010/11 Ningaloo Niño is primarily caused by the horizontal heat advection, which is evident in both the *control* and *no-shelf* experiments. The maximum heating due to horizontal heat advection occurs around September 2010, which is about 0.5°C $\text{month}^{-1}$ in the *control* experiment, and it is weaker in the *no-shelf* experiment, ~0.4°C $\text{month}^{-1}$ (Fig. 11d). Large differences are found

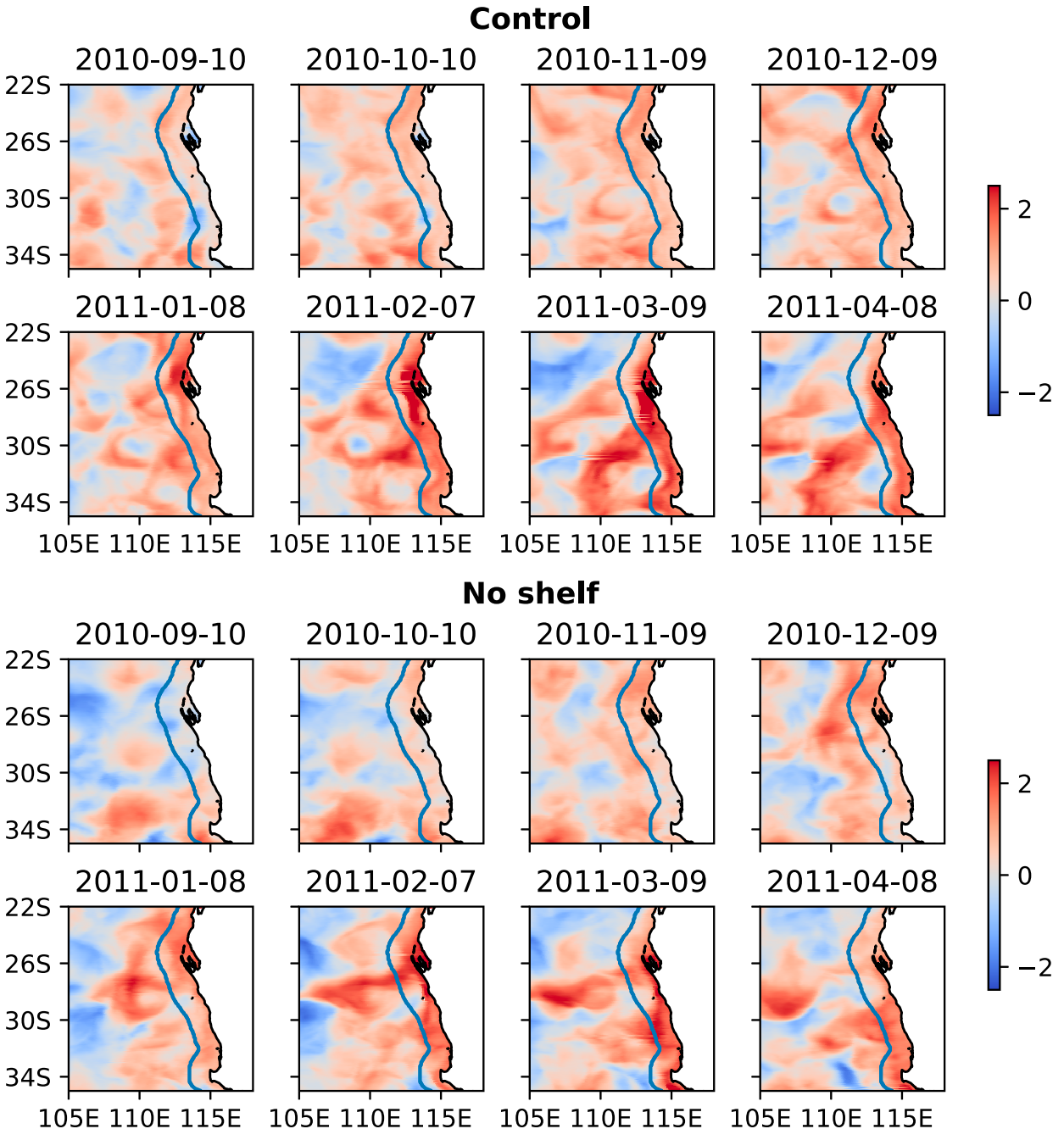


FIG. 10. SST anomalies (°C) during the 2010/11 Ningaloo Niño from the (top) *control* and (bottom) *no-shelf* experiments. The data have been smoothed with a 100-day lowpass filter. Blue lines denote the western edge of the LC (Fig. 1).

in the meridional heat advection. In the *control* experiment, positive meridional heat advection gradually increases since July, peaks in December 2010, and becomes negative in March 2011 (Fig. 11e). In the *no-shelf* experiment, it stays positive for only 3 months (October–December 2010). The zonal heat advection, in contrast, stays positive during the entire warming event (Fig. 11f), partly compensating for the reduced meridional heat advection. Figure 11h shows that the anomalous warming due to zonal heat advection in the *no-shelf* experiment is mainly caused by $u'T'_x$, which includes the contribution from the Rossby waves and mesoscale eddies. Since the zonal heat advection in the *control* experiment is smaller than that in the *no-shelf* experiment, the warmer upper ocean temperature (Fig. 11a) is largely due to the difference in meridional heat advection. From September 2010 to March 2011, the average temperature anomaly is 0.79°C for the *control* experiment

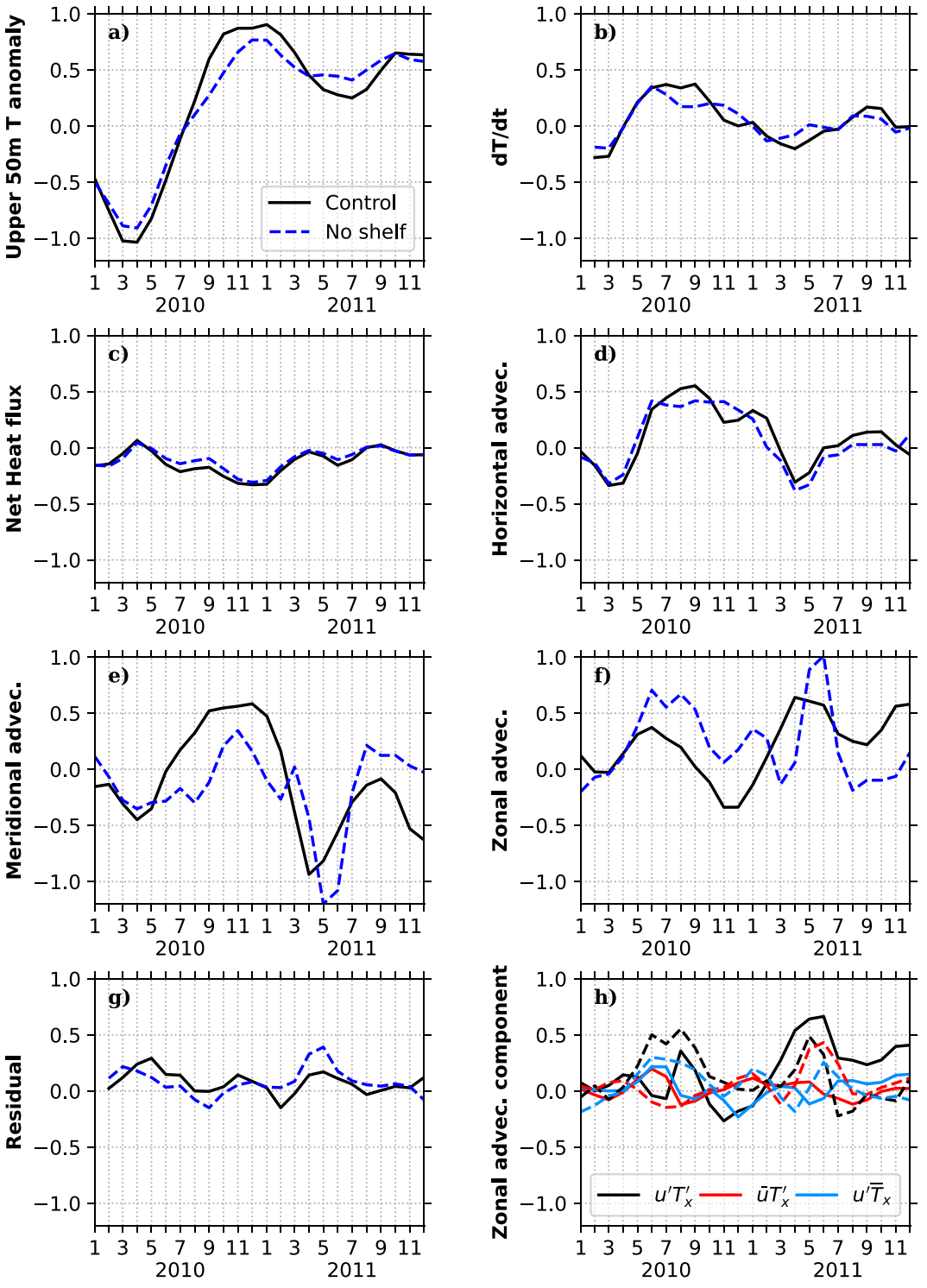


FIG. 11. The monthly (a) upper-50-m temperature anomaly (°C) and (b)–(h) anomalous heat budget terms (°C month$^{-1}$). The labels on the *y* axes show the heat budget terms. The data in the panels are averaged over the NNI region. The solid lines represent the *control* experiment, and the dashed lines represent the *no-shelf* experiment. The data used in Eq. (2) have been smoothed with a 100-day running-mean filter.

and 0.58°C for the *no-shelf* experiment, which is about a 26% reduction.

The net surface heat flux anomaly is negative in both experiments (Fig. 11c), and thus it does not contribute to the warming. Some previous studies suggest that the air–sea heat flux could partly contribute to the warming at the peak phase of the 2010/11 Ningaloo Niño (e.g., Feng et al. 2013; Marshall et al. 2015). However, the air–sea flux estimates in this region vary substantially with different datasets (Feng and Shinoda 2019), and thus the relative contributions of air–sea flux and LC-induced heat advection have uncertainties. The errors stemming from the air–sea flux formulation in the experiments might be partly responsible for the discrepancies between this study and previous estimates. Near the west coast of Australia, the residual term in the climatology heat budget is large during austral winter. For example, the residual provides ~1.3°C month$^{-1}$ warming tendency in July in the *control* experiment, which is a similar value reported in Marshall et al. (2015). However, the residual term is small (the absolute value is less than 0.2°C month$^{-1}$) during the warming phase of the 2010/11 Ningaloo Niño and the difference between the two experiments is negligible (Fig. 11g).

### c. *Physical processes: Role of the continental shelf on the Ningaloo Niño development*

The oceanic processes relevant to the role of the continental shelf-slope on the LC variability and their impact on Ningaloo Niño development are discussed in this section. The analysis in section 3b suggests that the strengthening of the LC in July–October 2010 is likely caused by the coastal trapped waves which are originated from the remote region. To detect the coastal trapped waves, SSH anomalies along the coast in the two experiments are analyzed.

Figure 12 shows SSH anomalies along the west coast of Australia during the 2010/11 Ningaloo Niño. The SSH anomalies are smoothed with a 13-day lowpass filter to remove the high frequency variability and noises. In the *control* experiment, positive SSH anomalies propagate counterclockwise along the northwest and west coast of Australia in July–October 2010 (Fig. 12, top), in which the phase speed is consistent with the coastal trapped wave theory (Wang and Mooers 1976; Huthnance 1978; Brink 1991). For example, the propagation speed of the strong signal in September 2010 is about 4.7 m s$^{-1}$. During other periods, the propagation speed somewhat differs presumably due to the change in ocean stability. Note that the local wind anomalies near the coast during this period change from southeasterlies to easterlies, and thus they cannot generate coastal sea level rise (Fig. 8). Following these sea level rise events along the coast, coastal trapped waves are detected during the peak phase in January–February 2011 (Fig. 12, bottom). During this period, northerly wind anomalies dominate the west coast of Australia (Fig. 8). Such wind anomalies cause Ekman convergence at the boundary, thereby initiating subsequent coastal trapped waves. Accordingly, the positive SSH anomalies are further enhanced and extended southward in association with the propagation of coastal trapped waves. It should be noted that from late August to early October, coastal trapped waves with higher frequencies are evident in the unfiltered anomalies (not shown), and they may also impact the longer time scale variability.

In the *no-shelf* experiment, the propagation of SSH anomalies along the coast is also evident. However, the amplitude and the propagation speed are different from those in the *control* experiment. During the developing period in July–October 2010, positive sea level anomalies at the northwest shelf propagate southward with the amplitude decaying quickly at the west coast. The propagation speed is of the order of 1 m s$^{-1}$, which roughly agrees with coastal Kelvin wave phase speed. During the peak phase in January–February 2011, positive SSH anomalies generated by local winds are present along the coast, but the amplitude is smaller than that in the *control* experiment. The presence of continental shelf in the *control* experiment allows the SSH fluctuation along the coast to be effectively trapped over the continental slope through the propagation of coastal trapped waves. Without such sloping bottom topography, coastal Kelvin waves are not able to trap the anomalous sea level at the coast and thus the SSH anomalies along the coast are weaker in the *no-shelf* experiment.

The analysis described above clearly demonstrates that the continental shelf-slope plays an essential role in trapping the high sea level at the coast. Without a continental shelf-slope, the high sea level signals will radiate offshore as Rossby waves. To detect the Rossby wave radiation, daily SSH anomalies from the *control* and *no-shelf* experiments are compared and shown in Fig. 13. Because mesoscale eddies are active off the western Australian coast (Morrow et al. 2004; Feng et al. 2005), the signal of eddies is removed by a spatial filter to isolate large-scale ocean circulation and variability including Rossby waves. Following Delman et al. (2018), an error function based spatial lowpass filter is applied to the daily SSH anomaly. The filter with the cutoff wavenumber of 7° wavelength is applied in the wavenumber domain in both zonal and meridional directions. Then, the same filter with the cutoff frequency of 100 days is applied in the time domain to remove shorter time scale signals. The resulting SSH anomaly is shown in Fig. 13 at an interval of 30 days.

Consistent with Fig. 12 (top), the southward propagation of the high sea level anomalies associated with coastal trapped waves during the developing period (August–November 2010) is evident in the *control* experiment (Fig. 13). Note that the high SSH anomalies along the coast are found in wider areas than the LC scale because of the use of the spatial filter. The high sea level along the coast generates a large cross-shore pressure gradient associated with the strong LC. In the *no-shelf* experiment, the spatial distribution of SSH anomaly reveals a smaller sea level rise in the nearshore region and more pronounced westward propagation from the coast. Because of the absence of trapping mechanism due to the continental shelf-slope in the *no-shelf* experiment, the signals of SSH anomaly at the coast radiate offshore as Rossby waves. Hence a lack of continental shelf-slope leads to a smaller sea level anomaly along the west coast and a weaker LC in the *no-shelf* experiment (Fig. 7).

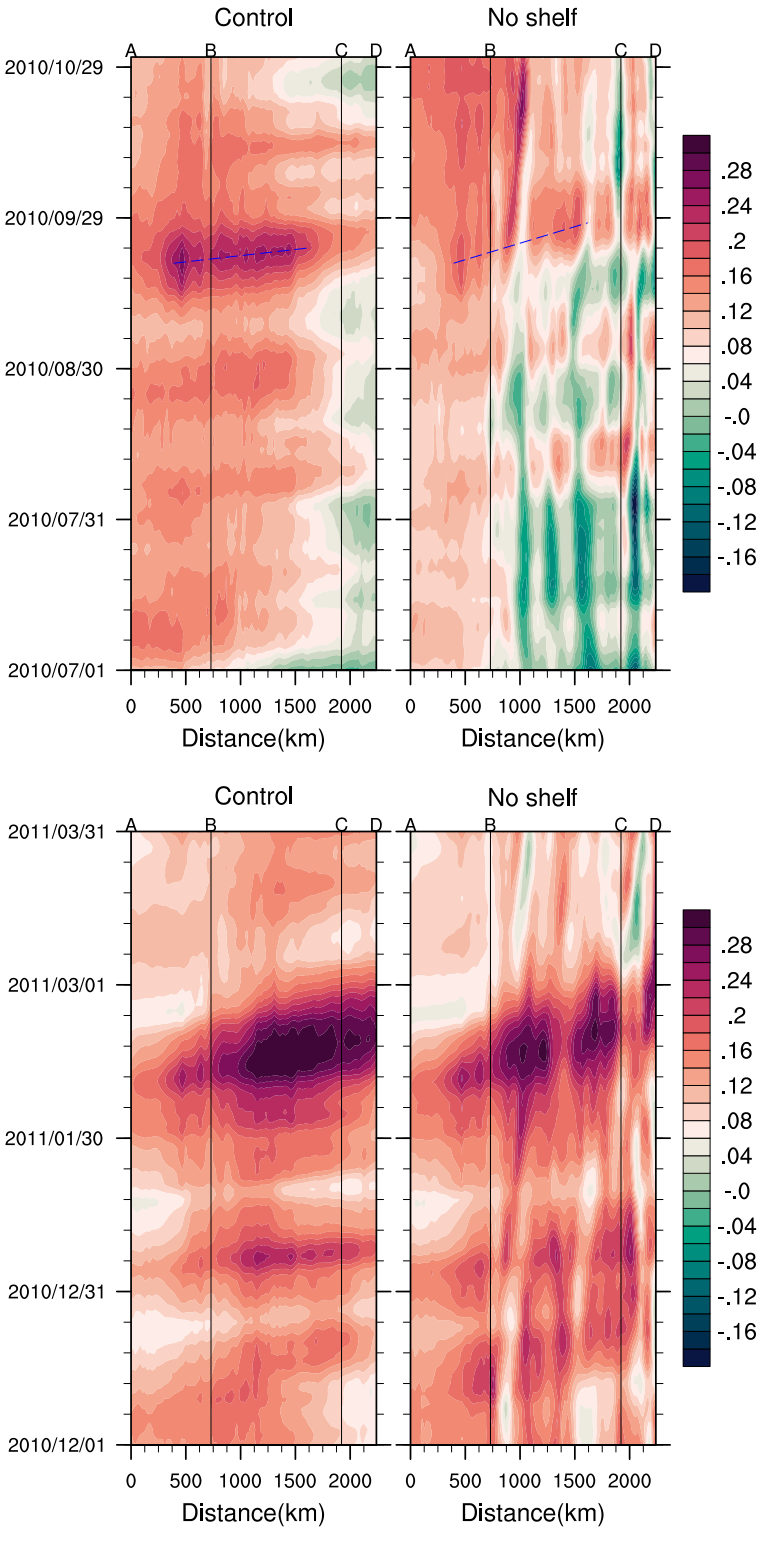


FIG. 12. SSH anomalies (m) along the coastal waveguide (the white line in Fig. 1) from the (left) *control* and (right) *no-shelf* experiments during (top) July–October 2010 and (bottom) December 2010–March 2011. The locations for points A–D are shown in Fig. 1. The black lines indicate the locations of 22° and 32°S. The blue dashed lines indicate phase lines of 4.7 m $s^{-1}$ (*control*) and 1.76 m $s^{-1}$ (*no-shelf*). The data have been smoothed with a 13-day running-mean filter.

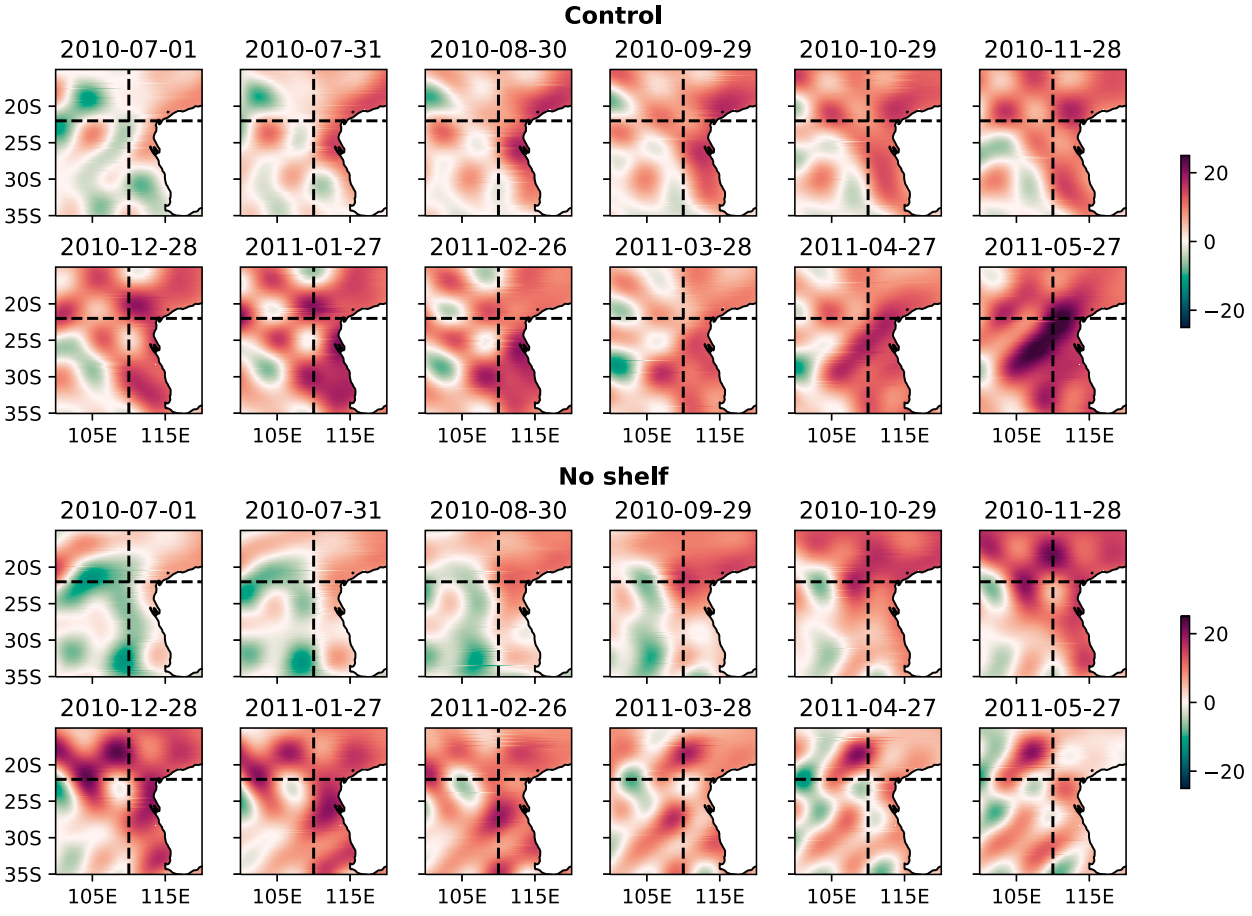


FIG. 13. SSH anomalies (cm) from the (top) *control* and (bottom) *no-shelf* experiments. The data have been spatially and temporally filtered. Horizontal dashed lines denote 22°S and vertical dashed lines denote 110°E.

In January 2011, the relatively high coastal sea level anomalies in response to the northerly wind anomalies are present in both experiments. While SSH anomalies in the *control* experiment remain trapped near the coast from February to March 2011, they radiate offshore as Rossby waves in the *no-shelf* experiment, resulting in smaller SSH anomalies at the coast. Therefore, the surge of the LC during the peak phase is weaker in the *no-shelf* experiment.

Hovmöller diagrams of SSH anomalies between 22° and 32°S from the model experiments and observations for the period 2011–14 are shown in Fig. 14 to further examine the westward propagation of the Rossby waves from the coast. During the 2010/11 Ningaloo Niño, SSH anomalies in the *control* experiment and observations are trapped near the coast, and positive SSH anomalies are mostly confined east of 110°E. On the other hand, the westward propagation of SSH disturbances with a phase speed of about 5 cm $s^{-1}$ is evident west of 110°E in the *no-shelf* experiment, which is consistent with the first baroclinic Rossby wave speed around these latitudes (Chelton and Schlax 1996).

Similar differences in SSH anomalies are also found during the 2011/12 Ningaloo Niño. For the 2012/13 Ningaloo Niño, however, the sea level rise along the west coast of Australia is smaller and the trapping of positive SSH anomalies is less obvious. This is because the maximum warming occurred near northwestern Australia north of 22°S in this event (Xu et al. 2018), and the LC enhancement is smaller than in the previous two warming events. Nevertheless, the westward propagation of Rossby waves is evident in the *no-shelf* experiment throughout the year, suggesting the considerable influence of continental shelf-slope on the overall ocean variability around Western Australia for a longer period.

To further quantify to what extent the topography near the west coast of Australia can effectively trap the Rossby wave energy at the coast, the standard deviation of SSH anomalies for the period from 2010 to 2014 is calculated (Fig. 15). The spatial pattern of the standard deviation in the *control* experiment agrees with observations reasonably well, although the magnitude is somewhat larger than the observation. While strong SSH variability near the coast rapidly weakens toward the open ocean in both the observation and the *control* experiment, it is much weaker in the nearshore region and stronger in the offshore region in the *no-shelf* experiment. The results further confirm the essential role of the continental shelf-slope in maintaining the coastal ocean variability by suppressing the radiation of Rossby waves.

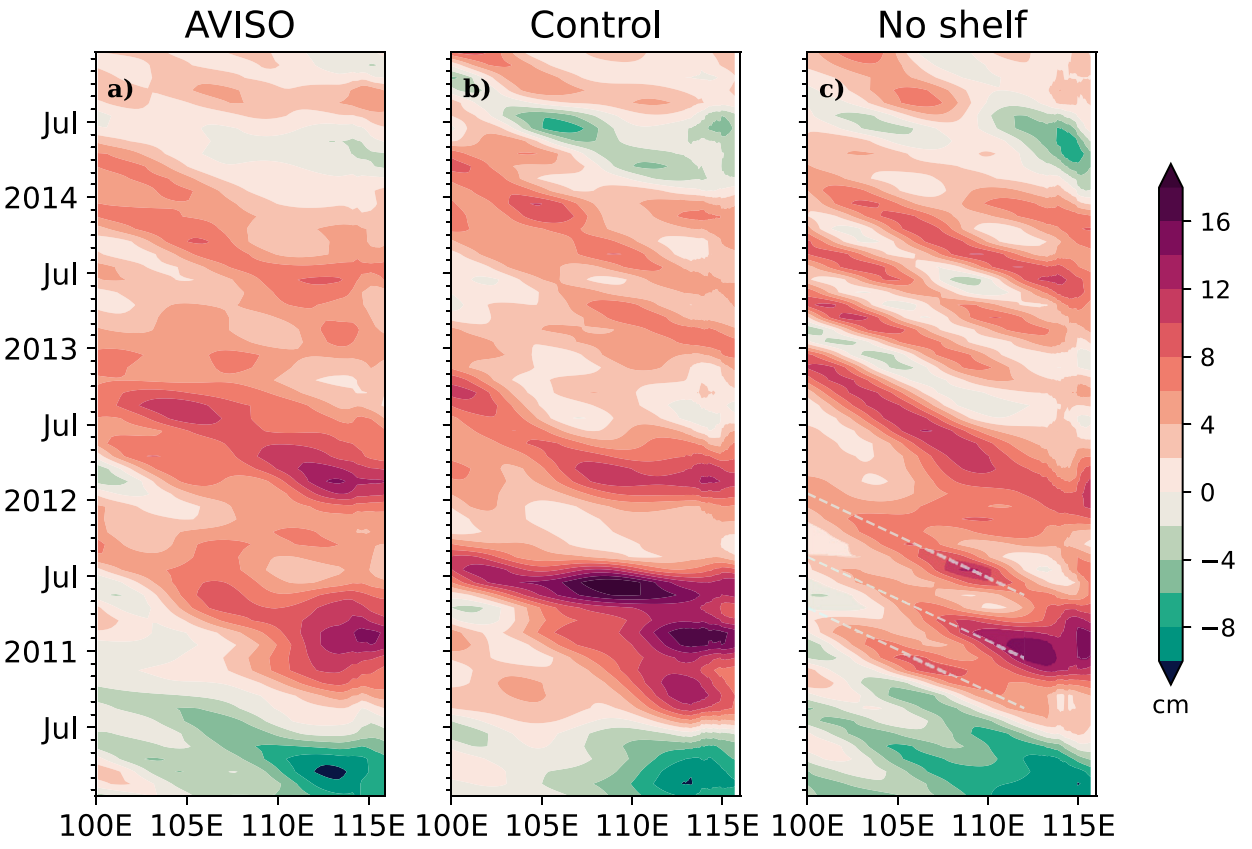


FIG. 14. Hovmöller diagrams for SSH anomalies (cm) averaged over 22°–32°S from (a) AVISO and from the (b) *control* and (c) *no-shelf* experiments. The data have been spatially and temporally filtered as in Fig. 13. White dashed lines are estimates for a zonal phase speed of 5.6 cm $s^{-1}$.

## 4. Summary and discussion

Previous theoretical studies based on idealized model experiments suggest that the presence of continental shelf-slope along the west coast of Australia plays a key role in generating a realistic LC. Using high-resolution Indo-Pacific basin OGCM experiments, this study investigates the effect of the topography on the LC and Ningaloo Niño. Two model experiments are designed to isolate the impact of continental shelf-slope on the LC. The *control* experiment uses realistic bottom topography, and the sensitivity experiment (*no-shelf* experiment) employs a modified topography in which the flat bottom (and thus no continental shelf and slope) is used near the coast.

The mean and variability of the LC are realistically simulated in the *control* experiment. While the vertical extent of the LC

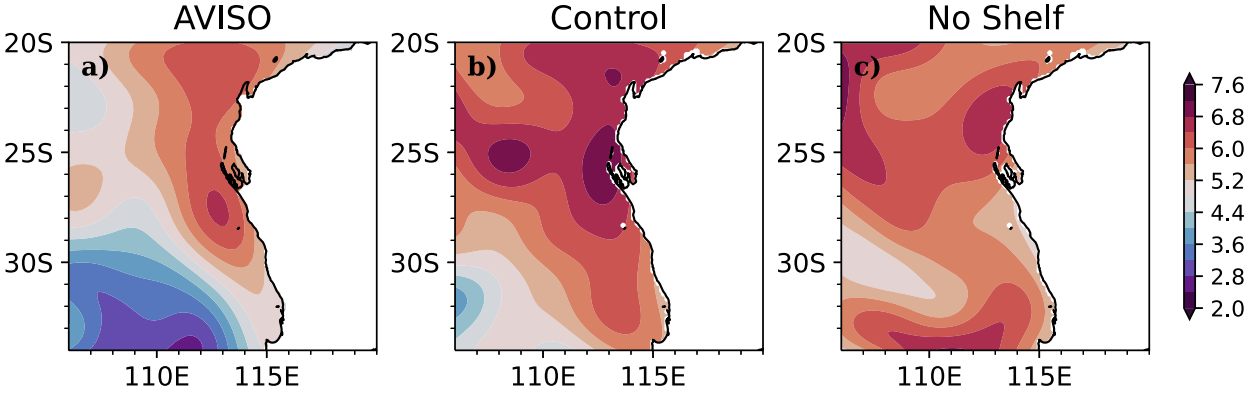


FIG. 15. The standard deviation of SSH anomalies (cm) from (a) AVISO and from the (b) *control*, and (c) *no-shelf* experiments. The data have been spatially and temporally filtered as in Fig. 13.

simulated by the *no-shelf* experiment is realistic, the magnitude is notably different from that in the *control* experiment. The composite of the LC between 22° and 34°S indicates that the core velocity in the *no-shelf* experiment is reduced by 28% on average over this latitudinal range. The reduction varies substantially with latitude, and the LC in the *no-shelf* experiment is about 40% weaker in the southern part around 34°S. The comparison of the two experiments suggests that the continental shelf-slope is an essential part of the LC dynamics as the topographic beta provides a trapping mechanism of the LC by suppressing the Rossby wave radiation from the coast, which is consistent with previous theoretical studies (Furue et al. 2013; Benthuysen et al. 2014b).

The significant influence of continental shelf-slope on LC variability is also evident during the 2010/11 Ningaloo Niño, which is associated with the surge of the LC. During this event, the enhancement of the LC begins in mid-2010, and peaks around September 2010 and February 2011, which is simulated well in the *control* experiment. In contrast, the enhancement of the LC is much weaker in the *no-shelf* experiment especially after July 2010, and the anomalous southward current is substantially weaker during August–October 2010 and January–February 2011 due to the absence of continental shelf and slope.

The surface warming in the *control* and *no-shelf* experiments also shows large differences during these two periods. The SST anomaly in the *control* experiment is about 0.5° and 0.3°C warmer than the *no-shelf* experiment in October 2010 and February 2011. The upper ocean heat budget analysis confirms that the temperature difference between the two experiments is primarily caused by the meridional heat advection. A stronger LC is generated in the *control* experiment due to the sloping bottom topography, resulting in larger meridional heat advection. The upper-50-m ocean temperature in the *control* experiment is 26% warmer than the *no-shelf* experiment during September 2010–March 2011.

Ocean dynamical processes during the 2010/11 Ningaloo Niño event are further examined by the analysis of SSH variations in the two experiments. The SSH evolution along the west coast of Australia during the event is realistically simulated in the *control* experiment. In the developing period from July to October 2010, the positive SSH anomalies along the west coast are associated with the propagation of remotely forced coastal trapped waves. At the peak phase, the SSH anomalies are further amplified by the Ekman convergence generated by anomalous northerly winds. Then the SSH anomalies are extended to the southern coast through the propagation of coastal trapped waves. The presence of the continental shelf-slope allows the SSH fluctuations to be trapped at the coast, and thus the positive SSH anomalies associated with the strong LC are sustained for a longer period. In contrast, positive SSH anomalies along the coast are much smaller in the *no-shelf* experiment because of the offshore radiation of Rossby waves from the coast. As a result, the anomalous LC in the *no-shelf* experiment is much weaker during most of the periods in the 2010/11 Ningaloo Niño.

This study demonstrates the important role of the continental shelf-slope in strengthening and trapping the LC and in the development of Ningaloo Niño. Since coarse-resolution ocean models generally underestimate the LC due to the inability to resolve its narrow width, they often underestimate the surface warming during the Ningaloo Niño (Doi et al. 2013; Zhang et al. 2018). The simulation of LC is substantially improved by the use of high-resolution ocean models (Furue 2019). While this is partly because models can resolve the narrow LC, mesoscale eddies, and bottom topography in key regions such as the Indonesian archipelago, this study suggests that the better representation of the bottom topography near the west coast of Australia in models is partly responsible for the realistic LC simulation. Hence the accurate representation of the continental shelf-slope near Western Australia is crucial for reducing the model's bias and for the prediction of major Ningaloo Niño such as the 2010/11 event, during which the LC enhancement plays a dominant role. Although the importance of the strengthening of LC by bottom topography for the development of the 2010/11 Ningaloo Niño is demonstrated in this study, it is likely that the effect largely depends on the event as processes that control the SST warming vary substantially from event to event (e.g., Marshall et al. 2015; Zhang et al. 2018). Careful evaluation and examination of ocean dynamical processes including the role of topographic trapping of LC in other Ningaloo Niño events are necessary for further improvement of simulation and prediction of LC and Ningaloo Niño.

*Acknowledgments.* The authors thank a reviewer Ryo Furue and another anonymous reviewer for their constructive comments that helped improve the manuscript. This research is supported by NSF Grant OCE-1658218. The computing resources are provided by HPC from Texas A&M University at College Station and Corpus Christi. TS is also supported by NOAA Grant NA17OAR4310256 and DOD Grant W911NF-20-1-0309. WH is supported by NSF OCE 1658132 and NASA OSTST 80NSSC21K1190.

*Data availability statement.* The ERA5 data were downloaded from the Copernicus Climate Change Service (C3S) Climate Data Store. The OAFlux dataset is available at https://oaflux.whoi.edu/data-access/. REMSS OI SST and TMI data are produced by Remote Sensing Systems and are available at www.remss.com. MUR SST analyses are available at https://doi.org/10.5067/GHGMR-4FJ04. OSTIA SST analyses are available at https://doi.org/10.5067/GHOST-4FK01. The NOAA OISST v2 data are provided by the NOAA/OAR/ESRL PSL, Boulder, Colorado, from their website at https://psl.noaa.gov/data/gridded/data.noaa.oisst.v2.highres.html. The sea level at Fremantle is from https://uhslc.soest.hawaii.edu/opendap/. The AVISO data are from https://www.aviso.altimetry.fr/en/data/products/sea-surface-height-products/global/gridded-sea-level-heights-and-derived-variables.html. The outputs of numerical model simulations conducted in this study are archived on the computing system at Texas A&M University—Corpus Christi, and are available upon request.

## REFERENCES

Benthuysen, J., M. Feng, and L. Zhong, 2014a: Spatial patterns of warming off western Australia during the 2011 Ningaloo

Niño: Quantifying impacts of remote and local forcing. *Cont. Shelf Res.*, **91**, 232–246, https://doi.org/10.1016/j.csr.2014.09.014.

——, R. Furue, J. P. J. McCreary, N. L. Bindoff, and H. E. Phillips, 2014b: Dynamics of the Leeuwin Current: Part 2. Impacts of mixing, friction, and advection on a buoyancy-driven eastern boundary current over a shelf. *Dyn. Atmos. Oceans*, **65**, 39–63, https://doi.org/10.1016/j.dynatmoce.2013.10.004.

Bleck, R., 2002: An oceanic general circulation model framed in hybrid isopycnic-Cartesian coordinates. *Ocean Modell.*, **4**, 55–88, https://doi.org/10.1016/S1463-5003(01)00012-9.

Brink, K., 1991: Coastal-trapped waves and wind-driven currents over the continental shelf. *Annu. Rev. Fluid Mech.*, **23**, 389–412, https://doi.org/10.1146/annurev.fl.23.010191.002133.

Chelton, D. B., and M. G. Schlax, 1996: Global observations of oceanic Rossby waves. *Science*, **272**, 234–238, https://doi.org/10.1126/science.272.5259.234.

Cresswell, G. R., and T. J. Golding, 1980: Observations of a south-flowing current in the southeastern Indian Ocean. *Deep-Sea Res.*, **27A**, 449–466, https://doi.org/10.1016/0198-0149(80)90055-2.

Delman, A. S., T. Lee, and B. Qiu, 2018: Interannual to multidecadal forcing of mesoscale eddy kinetic energy in the subtropical southern Indian Ocean. *J. Geophys. Res. Oceans*, **123**, 8180–8202, https://doi.org/10.1029/2018JC013945.

Deremble, B., N. Wienders, and W. K. Dewar, 2013: CheapAML: A simple, atmospheric boundary layer model for use in ocean-only model calculations. *Mon. Wea. Rev.*, **141**, 809–821, https://doi.org/10.1175/MWR-D-11-00254.1.

Doi, T., S. K. Behera, and T. Yamagata, 2013: Predictability of the Ningaloo Niño/Niña. *Sci. Rep.*, **3**, 2892, https://doi.org/10.1038/srep02892.

Donlon, C. J., M. Martin, J. Stark, J. Roberts-Jones, E. Fiedler, and W. Wimmer, 2012: The Operational Sea Surface Temperature and Sea Ice Analysis (OSTIA) system. *Remote Sens. Environ.*, **116**, 140–158, https://doi.org/10.1016/j.rse.2010.10.017.

Feng, M., G. Meyers, A. Pearce, and S. Wijffels, 2003: Annual and interannual variations of the Leeuwin Current at 32°S. *J. Geophys. Res.*, **108**, 3355, https://doi.org/10.1029/2002JC001763.

——, S. Wijffels, S. Godfrey, and G. Meyers, 2005: Do eddies play a role in the momentum balance of the Leeuwin Current? *J. Phys. Oceanogr.*, **35**, 964–975, https://doi.org/10.1175/JPO2730.1.

——, M. J. McPhaden, S.-P. Xie, and J. Hafner, 2013: La Niña forces unprecedented Leeuwin Current warming in 2011. *Sci. Rep.*, **3**, 1277, https://doi.org/10.1038/srep01277.

Feng, X., and T. Shinoda, 2019: Air-sea heat flux variability in the southeast Indian Ocean and its relation with Ningaloo Niño. *Front. Mar. Sci.*, **6**, 266, https://doi.org/10.3389/fmars.2019.00266.

Furue, R., 2019: The three-dimensional structure of the Leeuwin Current System in density coordinates in an eddy-resolving OGCM. *Ocean Modell.*, **138**, 36–50, https://doi.org/10.1016/j.ocemod.2019.03.001.

——, J. P. McCreary, J. Benthuysen, H. E. Phillips, and N. L. Bindoff, 2013: Dynamics of the Leeuwin Current: Part 1. Coastal flows in an inviscid, variable-density, layer model. *Dyn. Atmos. Oceans*, **63**, 24–59, https://doi.org/10.1016/j.dynatmoce.2013.03.003.

——, K. Guerreiro, H. E. Phillips, J. P. J. McCreary, and N. L. Bindoff, 2017: On the Leeuwin Current System and its linkage to zonal flows in the south Indian Ocean as inferred from a gridded hydrography. *J. Phys. Oceanogr.*, **47**, 583–602, https://doi.org/10.1175/JPO-D-16-0170.1.

Godfrey, J. S., and K. R. Ridgway, 1985: The large-scale environment of the poleward-flowing Leeuwin Current, western Australia: Longshore steric height gradients, wind stresses, and geostrophic flow. *J. Phys. Oceanogr.*, **15**, 481–495, https://doi.org/10.1175/1520-0485(1985)015<0481:TLSEOT>2.0.CO;2.

——, and A. J. Weaver, 1991: Is the Leeuwin Current driven by Pacific heating and winds? *Prog. Oceanogr.*, **27**, 225–272, https://doi.org/10.1016/0079-6611(91)90026-I.

Hersbach, H., Coauthors, 2018: ERA5 hourly data on single levels from 1979 to present. Copernicus Climate Change Service (C3S) Climate Data Store (CDS), accessed 20 July 2019, https://doi.org/10.24381/cds.adbb2d47.

Huthnance, J. M., 1978: On coastal trapped waves: Analysis and numerical calculation by inverse iteration. *J. Phys. Oceanogr.*, **8**, 74–92, https://doi.org/10.1175/1520-0485(1978)008<0074:OCTWAA>2.0.CO;2.

Kataoka, T., T. Tozuka, and T. Yamagata, 2017: Generation and decay mechanisms of Ningaloo Niño/Niña. *J. Geophys. Res. Oceans*, **122**, 8913–8932, https://doi.org/10.1002/2017JC012966.

Kundu, P. K., and J. P. J. McCreary, 1986: On the dynamics of the throughflow from the Pacific into the Indian Ocean. *J. Phys. Oceanogr.*, **16**, 2191–2198, https://doi.org/10.1175/1520-0485(1986)016<2191:OTDOTT>2.0.CO;2.

Large, W. G., and S. Yeager, 2004: Diurnal to decadal global forcing for ocean and sea-ice models: The data sets and flux climatologies. NCAR Tech. Note NCAR/TN-460+STR, University Corporation for Atmospheric Research, 105 pp., https://doi.org/10.5065/D6KK98Q6.

Marshall, A. G., H. H. Hendon, M. Feng, and A. Schiller, 2015: Initiation and amplification of the Ningaloo Niño. *Climate Dyn.*, **45**, 2367–2385, https://doi.org/10.1007/s00382-015-2477-5.

McCreary, J. P. J., S. R. Shetye, and P. K. Kundu, 1986: Thermohaline forcing of eastern boundary currents: With application to the circulation off the west coast of Australia. *J. Mar. Res.*, **44**, 71–92, https://doi.org/10.1357/002224086788460184.

Metzger, E. J., H. E. Hurlburt, X. Xu, J. F. Shriver, A. L. Gordon, J. Sprintall, R. D. Susanto, and H. M. van Aken, 2010: Simulated and observed circulation in the Indonesian Seas: 1/12° global HYCOM and the INSTANT observations. *Dyn. Atmos. Oceans*, **50**, 275–300, https://doi.org/10.1016/j.dynatmoce.2010.04.002.

Morrow, R., F. Birol, D. Griffin, and J. Sudre, 2004: Divergent pathways of cyclonic and anti-cyclonic ocean eddies. *Geophys. Res. Lett.*, **31**, L24311, https://doi.org/10.1029/2004GL020974.

Pearce, A. F., and M. Feng, 2013: The rise and fall of the "marine heat wave" off Western Australia during the summer of 2010/2011. *J. Mar. Syst.*, **111–112**, 139–156, https://doi.org/10.1016/j.jmarsys.2012.10.009.

Reynolds, R. W., T. M. Smith, C. Liu, D. B. Chelton, K. S. Casey, and M. G. Schlax, 2007: Daily high-resolution-blended analyses for sea surface temperature. *J. Climate*, **20**, 5473–5496, https://doi.org/10.1175/2007JCLI1824.1.

Seager, R., M. B. Blumenthal, and Y. Kushnir, 1995: An advective atmospheric mixed layer model for ocean modeling purposes: Global simulation of surface heat fluxes. *J. Climate*, **8**, 1951–1964, https://doi.org/10.1175/1520-0442(1995)008<1951:AAAMLM>2.0.CO;2.

Shinoda, T., and J. Lin, 2009: Interannual variability of the upper ocean in the southeast Pacific stratus cloud region. *J. Climate*, **22**, 5072–5088, https://doi.org/10.1175/2009JCLI2696.1.

Smith, R. L., A. Huyer, J. S. Godfrey, and J. Church, 1991: The Leeuwin Current off western Australia, 1986–1987. *J. Phys. Oceanogr.*, **21**, 323–345, https://doi.org/10.1175/1520-0485(1991)021<0323:TLCOWA>2.0.CO;2.

Steele, M., R. Morley, and W. Ermold, 2001: PHC: A global ocean hydrography with a high-quality Arctic Ocean. *J. Climate*, **14**, 2079–2087, https://doi.org/10.1175/1520-0442(2001)014<2079:PAGOHW>2.0.CO;2.

Thompson, R., 1984: Observations of the Leeuwin Current off Western Australia. *J. Phys. Oceanogr.*, **14**, 623–628, https://doi.org/10.1175/1520-0485(1984)014<0623:OOTLCO>2.0.CO;2.

Waliser, D. E., and N. E. Graham, 1993: Convective cloud systems and warm-pool sea surface temperatures: Coupled interactions and self-regulation. *J. Geophys. Res.*, **98**, 12 881–12 893, https://doi.org/10.1029/93JD00872.

Wang, D.-P., and C. N. K. Mooers, 1976: Coastal-trapped waves in a continuously stratified ocean. *J. Phys. Oceanogr.*, **6**, 853–863, https://doi.org/10.1175/1520-0485(1976)006<0853:CTWIAC>2.0.CO;2.

Weatherall, P., and Coauthors, 2015: A new digital bathymetric model of the world's oceans. *Earth Space Sci.*, **2**, 331–345, https://doi.org/10.1002/2015EA000107.

Weaver, A. J., and J. H. Middleton, 1989: On the dynamics of the Leeuwin Current. *J. Phys. Oceanogr.*, **19**, 626–648, https://doi.org/10.1175/1520-0485(1989)019<0626:OTDOTL>2.0.CO;2.

——, and ——, 1990: An analytic model for the Leeuwin Current off Western Australia. *Cont. Shelf Res.*, **10**, 105–122, https://doi.org/10.1016/0278-4343(90)90025-H.

Wernberg, T., D. A. Smale, F. Tuya, M. S. Thomsen, T. J. Langlois, T. De Bettignies, S. Bennett, and C. S. Rousseaux, 2013: An extreme climatic event alters marine ecosystem structure in a global biodiversity hotspot. *Nat. Climate Change*, **3**, 78–82, https://doi.org/10.1038/nclimate1627.

Xu, J., R. J. Lowe, G. N. Ivey, N. L. Jones, and Z. Zhang, 2018: Contrasting heat budget dynamics during two La Niña marine heat wave events along northwestern Australia. *J. Geophys. Res. Oceans*, **123**, 1563–1581, https://doi.org/10.1002/2017JC013426.

Yu, L., X. Jin, and R. A. Weller, 2008: Multidecade Global Flux Datasets from the Objectively Analyzed Air-sea Fluxes (OAFlux) Project: Latent and sensible heat fluxes, ocean evaporation, and related surface meteorological variables. Woods Hole Oceanographic Institution, OAFlux Project Tech. Rep. OA-2008-01, 64 pp., https://rda.ucar.edu/datasets/ds260.1/docs/OAFlux_TechReport_3rd_release.pdf.

Zhang, L., W. Han, Y. Li, and T. Shinoda, 2018: Mechanisms for generation and development of Ningaloo Niño. *J. Climate*, **31**, 9239–9259, https://doi.org/10.1175/JCLI-D-18-0175.1.